Mapping methane point emissions with the PRISMA spaceborne imaging spectrometer

Luis Guanter [a,*], Itziar Irakulis-Loitxate [a], Javier Gorroño [a], Elena Sánchez-García [a], Daniel H. Cusworth [b], Daniel J. Varon [c], Sergio Cogliati [d], Roberto Colombo [d]

[a] *Research Institute of Water and Environmental Engineering (IIAMA), Universitat Politècnica de València, Valencia, Spain*
[b] *Jet Propulsion Laboratory, California Institute of Technology, Pasadena, CA, USA*
[c] *School of Engineering and Applied Science, Harvard University, Cambridge, MA, USA*
[d] *Remote Sensing of Environmental Dynamics Laboratory, Department of Environmental and Earth Sciences, University of Milano - Bicocca, Milano, Italy*

Abstract

The detection of methane emissions from fossil fuel production activities, such as oil and gas extraction and coal mining, has been identified as a key means for the reduction of greenhouse gas emissions to the atmosphere. Several types of optical satellite sensors have recently been shown to be instrumental for this task. Spaceborne imaging spectrometers belong to this group. These instruments measure the solar radiation reflected by the Earth in hundreds of spectral channels in the 400-2500 nm spectral range with a typical spectral resolution of 10 nm and a spatial resolution of 30 m. The Italian PRISMA mission is the first system of this type providing data openly to the international scientific community. In this work, we evaluate the potential of PRISMA for methane mapping. Our retrieval of methane concentration enhancements is based on a matched-filter based algorithm applied to the 2300 nm spectral region containing methane absorption bands. We perform a simulation-based sensitivity analysis to assess the retrieval performance for different sites. The impact on the retrieval of uncertainties in PRISMA's spectral response and of different illumination conditions has also been evaluated. We find that brightness and homogeneity of the surface are major drivers for the detection and quantification of methane plumes with PRISMA, with precision errors ranging from 61 to 197 ppb in the evaluated images. The potential of PRISMA for methane mapping is further illustrated by real plume detections at different methane hotspot regions, including oil and gas extraction fields in Algeria, Turkmenistan, and the Permian Basin (USA) as well as the coal mines in the Shanxi region in China. Our study reports several important findings regarding the potential and limitations of PRISMA for methane mapping, most of which can be extrapolated to upcoming satellite imaging spectroscopy missions.

Key words: Methane retrieval, PRISMA satellite mission, imaging spectroscopy, point emissions, spectral calibration

1. Introduction

Methane (CH_4) emissions from fossil fuel production have been found to account for 35% (range 30%–42%) of total global anthropogenic emissions (Saunois et al., 2020). Emissions mostly originate from oil and gas production infrastructure, such as wells, gathering stations, compressor stations, storage tanks, pipelines, processing plants, and flares (Lyon et al., 2016), but also coal mines can be strong methane emitters. These industrial methane emissions typically happen as so-called "point emissions", namely plumes emitted from small surface elements and containing a relatively large amount of gas (Duren et al., 2019). The detection and elimination of unintended methane emissions from fossil fuel production activities have been identified as a key means to reduce the concentration of greenhouse gases in the atmosphere (United Nations Environment Programme, 2021).

Satellites offer a unique capability for global monitoring of methane emissions (Jacob et al., 2016). The retrieval of methane from space measurements typically relies on spectrally-resolved measurements of solar radiation reflected by the Earth's surface in the shortwave infrared (SWIR) part of the spectrum (∼1600–2500 nm). Methane presents two absorption bands in this region, a weaker

* Corresponding author.
Email address: lguanter@fis.upv.es (Luis Guanter).

one around 1700 nm and a stronger one around 2300 nm. Carbon dioxide, nitrous oxide and especially water vapor also present optical activity in the SWIR (see Fig. 1). The flagship satellite mission for global methane monitoring is the TROPOspheric Monitoring Instrument (TROPOMI) onboard the Copernicus Sentinel-5 Precursor satellite (Veefkind et al., 2012). TROPOMI provides accurate methane column concentration (XCH_4) data derived from its high spectral resolution SWIR channel with a $7\times7\,km^2$ spatial sampling ($7.0\times5.5\,km^2$ since August 2019) and global daily coverage. However, despite TROPOMI's unprecedented high performance for methane monitoring, its relatively coarse spatial sampling limits its application to the detection of regional methane hotspots (e.g. Cusworth et al., 2018; Zhang et al., 2020; Schneising et al., 2020; Barré et al., 2020; de Gouw et al., 2020) or to the strongest points emissions (e.g. Pandey et al., 2019; Varon et al., 2019).

Fortunately, a number of satellite missions able to map methane point emissions are currently operating. The GHGSat private constellation (3 satellites at the moment) was designed for methane retrieval and has been leading the field of satellite-based high-resolution methane mapping in the last years (Varon et al., 2019, 2020a). The Fourier-transform spectrometers onboard the GHGSat satellites sample the 1700 nm methane band with a high spectral resolution, a swath of ∼12 km and a spatial sampling of either 50 or 25 m, depending on the satellite (Jervis et al., 2021). Restricted data access and the low spatio-temporal coverage might be the main limitations for the use of GHGSat data by the scientific community.

Complementary to GHGSat, so-called imaging spectrometers (also known as hyperspectral imagers) are increasingly demonstrating their potential for methane mapping. These instruments cover the solar spectrum (∼400-2500 nm) with a typical spectral resolution of 5–10 nm, and a 30 m spatial sampling in the case of spaceborne instruments. Even though they are not optimized for methane mapping, they sample the strong methane absorption at 2300 nm with tens of spectral channels, which can be exploited for methane retrieval. The development of this application of optical imaging spectrometers has relied on a number of airborne campaigns using the AVIRIS and AVIRIS-NG instruments operated by the Jet Propulsion Laboratory in the U.S. (e.g. Roberts et al., 2010; Thorpe et al., 2014; Thompson et al., 2015), including several large-scale campaigns (Frankenberg et al., 2016; Duren et al., 2019; Cusworth et al., 2020). The potential of satellite-based imaging spectrometers for methane mapping was first shown by Thompson et al. (2016), who used data from the Hyperion technology demonstrator to map the massive emissions from the Aliso Canyon disaster. Simulation-based studies of the potential of spaceborne spectrometers for methane retrieval are presented in Cusworth et al. (2019) and Ayasse et al. (2019). However, progress in the use of spaceborne spectrometers for methane mapping has been limited so far because of the lack of suitable data.

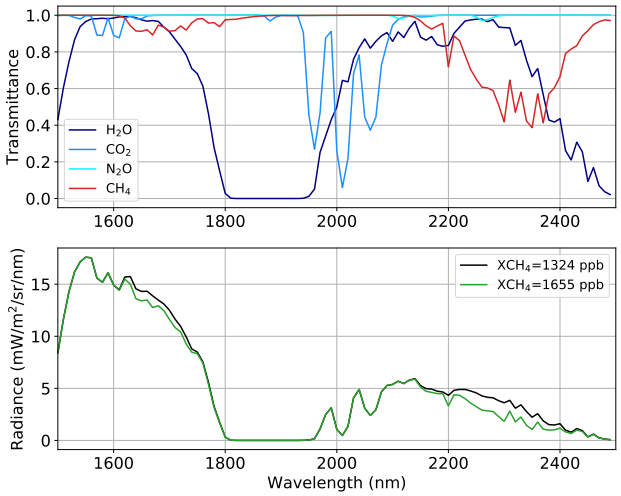

Fig. 1. Sensitivity of PRISMA SWIR measurements to methane. Top, two-way transmittance of the gases with the highest absorption in the SWIR part of the spectrum. Bottom, simulated top-of-atmosphere radiance spectra in the SWIR as measured by PRISMA, for two different methane column concentrations (XCH_4).

This situation has changed since the launch of the PRISMA (PRecursore IperSpettrale della Missione Applicativa) mission by the Italian Space Agency on 22 March 2019 (Cogliati et al., 2021). PRISMA generates open-access images with a swath of 30 km, a 30 m spatial sampling and a ∼10 nm spectral resolution in the 2300 nm region. These characteristics make PRISMA to be the only imaging spectrometer with potential for high resolution methane mapping currently accessible to the international science community. The first study using methane retrievals from PRISMA is the one by Cusworth et al. (2021), which combined PRISMA data with a number of other remote sensing data sets to quantify methane emissions from a gas well blowout in Texas (USA). In addition to PRISMA, the Advanced Hyperspectral Imagers (AHSI) onboard the Chinese Gaofen-5 and ZY1 satellite can also be used for methane monitoring (Irakulis-Loitxate et al., 2021), but the data are in general not accessible to the broad scientific community. Finally, the Sentinel-2 and Landsat multispectral missions have recently been shown to be useful to map strong methane emissions when those occur over bright and spatially homogeneous areas (Varon et al., 2020b), although the detection limits of multispectral imagers for single emissions remain much higher than those of GHGSat and imaging spectrometers because of the substantially poorer spectral information.

In this study, we evaluate the potential of PRISMA for the detection and quantification of methane point emissions from fossil fuel production activities. We rely on an end-to-end sensitivity analysis to assess retrieval uncertainties and detection limits over different surfaces. The potential of PRISMA for methane mapping is further illustrated by the presentation of a number of plumes derived from PRISMA data over oil and gas production basins in Algeria, Turkmenistan, and USA, and a coal mining region in China.

2. Materials and Methods

2.1. *Methane retrieval*

In the case of high spatial resolution methane mapping from space measurements, the retrieval target variable is in general the per-pixel enhancement of methane column concentration with respect to the background (ΔXCH_4).

Both physically-based and data-driven methods have been used for ΔXCH_4 retrieval with imaging spectroscopy data. Physically-based methods rely on the explicit modelling of the radiative transfer between the surface, atmosphere and instrument. The family of differential optical absorption spectroscopy (DOAS) methods belong to that group and have been used with AVIRIS and AVIRIS-NG airborne data (e.g. Thorpe et al., 2017; Borchardt et al., 2020). As an alternative, data-driven methods constrain the retrieval with information extracted from the image by means of statistical methods. For example, data-driven methane retrievals based on the matched-filter and the singular vector decomposition concepts have been successfully used with imaging spectroscopy data (Thorpe et al., 2014; Thompson et al., 2015, 2016; Foote et al., 2020). For this study, we choose a basic matched-filter retrieval. The reasons for this choice are its superior computational efficiency to physically-based methods, and the fact that it can implicitly account for potential radiometric and spectral errors, which are likely to happen in satellite data. Also, matched-filter retrievals directly provide the sought ΔXCH_4 estimates, unlike physically based methods which provide only XCH_4.

The matched-filter retrieval is based on the idea that each input spectrum can be expressed as the perturbation of an average radiance spectrum by a change in the methane column concentration. This is modelled as a so-called target spectrum, which represents the radiative transfer signal of a unit methane absorption. Our formulation of the matched-filter retrieval is similar to the one used by Thompson et al. (2016) with Hyperion. If we name ΔXCH_4 as $\widehat{\alpha}$, the matched-filter takes the form

$$\widehat{\alpha}(\boldsymbol{x}) = \frac{(\boldsymbol{x}-\boldsymbol{\mu})^T \Sigma^{-1} \boldsymbol{t}}{\boldsymbol{t}^T \Sigma^{-1} \boldsymbol{t}}, \qquad (1)$$

where $\boldsymbol{x}$ is the spectrum under analysis, $\boldsymbol{\mu}$ and Σ are the mean and covariance of the background radiance, and $\boldsymbol{t}$ is the target spectrum representing the perturbation of the background radiance signal by a methane enhancement. The $\boldsymbol{t}$ spectrum has units of radiance over methane column concentration, and is generated as $\boldsymbol{\mu} \cdot \boldsymbol{k}$, with $\boldsymbol{k}$ being a unit methane absorption spectrum calculated using radiative transfer simulations. An example of a $\boldsymbol{k}$ target unit absorption spectrum is shown in Fig. 2. The variables $\boldsymbol{\mu}$ and Σ are calculated on a per-column basis in order to account for the different radiometric responses of detector elements across-track. In the case of the target spectrum, one single instance of $\boldsymbol{t}$ is generated at high spectral resolution for the entire image considering the illumination and observation angles of the acquisition, but the spectral convolution with the PRISMA spectral response function is performed on a per-column basis in order to account for potential across-track variations of the instrument spectral response (see Sec. 2.2). The 2110–2450 nm window is selected for the matched-filter retrieval. Other narrower fitting windows were tested, but they yielded higher precision errors without a clear gain in retrieval accuracy.

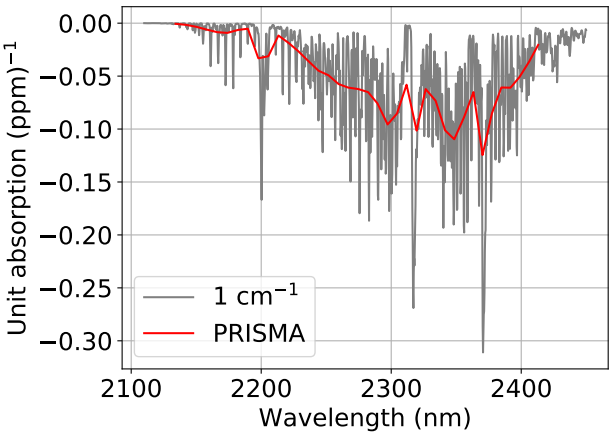

Fig. 2. Example of a unit methane absorption spectrum $\boldsymbol{k}$ used as target signature by the matched filter retrieval method used in this study.

The basic version of the matched-filter that we have chosen is relatively sensitive to measurement noise and to changes in the surface albedo. The MAG1C code (Matched filter with Albedo correction and reweiGhted L1 sparsity Code) was designed to overcome those difficulties through the addition of a sparsity assumption and an albedo correction (Foote et al., 2020). We have tested the performance of both the basic matched-filter retrieval and MAG1C for the processing of PRISMA data in this work (see Sec. 3.2 and Fig. 13).

2.2. *Spectral characterization*

An accurate knowledge of the instrument's spectral response is required for spectroscopic applications dealing with sharp absorption features, such as those from atmospheric absorptions involved in methane retrieval (Green, 1998). An initial pre-processing step in our retrieval updates the nominal spectral calibration parameters around the 2300 nm attached to the PRISMA images. This is achieved through scene-based methods in which the channel wavelength center and width are updated for each across-track position in the image. The algorithm utilized for this purpose is similar to others already in the literature (e.g. Gao et al., 2004; Green et al., 2003; Guanter et al., 2006; Brazile et al., 2008; Guanter et al., 2009b). These search for the spectral channel position, and in some cases also width, leading to the best fit between modelled and reference image spectra.

The method adapted to PRISMA SWIR data in this

work starts by generating a set of across-track reference spectra with an enhanced signal-to-noise ratio (SNR). Each across-track reference spectrum is derived through averaging top-of-atmosphere (TOA) radiance spectra in the same image column. The channel position and width of each input reference spectrum is then estimated through an iterative optimization process, fitting modelled spectra to the reference spectra. The 2280–2380 nm window, affected by methane and water vapor absorption lines, is chosen for the inversion. For each iteration, radiance spectra are modelled as the combination of high spectral resolution atmospheric transmittance functions derived from radiative transfer simulations, and spectral surface reflectance represented by a third order polynominal in wavelength. The modelled high-resolution TOA radiance spectrum calculated as the product of atmospheric transmittance and surface reflectance is convoluted with the instrument's spectral response function for varying values of the channel center wavelength and full-width at half-maximum (FWHM) of a Gaussian function. These two parameters are optimized together with the weights of the polynomial terms in the inversion process. This is performed for all samples in the across-track direction in order to determine center wavelength and width curves for the 2300 nm spectral region of interest for methane retrievals.

2.3. *Detection of plumes in ΔXCH_4 maps*

Our detection of methane plumes in the ΔXCH$_4$ maps produced from PRISMA data is based on visual inspection. The reason not to implement an automatic plume detection method is that the ΔXCH$_4$ maps from PRISMA contain a substantial amount of both normally-distributed noise (propagated from measurement noise) and spatially-coherent retrieval artifacts correlated with surface features which disturb the retrieval. The latter make it difficult to develop automatic plume detection methods.

After the geometric correction of the ΔXCH$_4$ maps, these are co-located with wind speed data and very high spatial resolution true color images of the area (e.g. from Google Earth or Bing maps applications). The supervised plume detection approach searches for spatial patterns with the typical shape of a gas plume, namely high ΔXCH$_4$ values progressively decreasing downwind. The candidate plumes identified through a first screening based on visual inspection are compared with the input spectral radiance data at 2300 nm to discard false positives due to surface patterns. Then, the resulting plume candidates are confronted with wind and very high resolution images. The candidate plume is considered to be a real one if it aligns with the wind direction and originates at a point where potentially-emitting infrastructure is located according to the high resolution data.

2.4. *Estimation of emission flux rates*

Emission flux rate (Q) values in kilograms per hour (kg/h) are calculated for each detected plume in the last processing step. We manually define a polygon to isolate the plume from the background. The calculation of Q from pixel-wise ΔXCH$_4$ values in the plume is done using the so-called integrated methane enhancement (IME) model (Frankenberg et al., 2016; Varon et al., 2018). We calculate an IME in kg units as the total excess mass of methane contained in the plume (Frankenberg et al., 2016),

$$\mathrm{IME} = k \sum_{i=1}^{n_p} \widehat{\alpha}(i), \tag{2}$$

where n_p is the number of pixels in the plume and k is a scaling factor converting the total of pixel-wise methane concentration values to kg by assuming Avogadro's law and taking into account the pixel size and the molecular weight of methane. Q is then calculated as

$$Q = \frac{U_{\mathrm{eff}} \cdot \mathrm{IME}}{L}, \tag{3}$$

where U_{eff} is an effective wind speed and L the plume length scale (square root of the plume mask area). The U_{eff} term is calculated from the measurable 10-m wind speed U_{10} as

$$U_{\mathrm{eff}} = 0.34 \cdot U_{10} + 0.44. \tag{4}$$

This relationship was derived using large-eddy simulations specifically performed for a spatial resolution and ΔXCH$_4$ retrieval precision compatible with the PRISMA data using the methodology described in Varon et al. (2018). U_{10} data are taken from the GEOS-FP data set (Molod et al., 2012) for the nearest time and location of each detected plume.

Uncertainties in Q are estimated using an error propagation scheme similar to the one proposed by Cusworth et al. (2020). We propagate random errors in IME and U_{10} to a 1-σ precision error in Q. The U_{10} term is the dominant error contribution. A 50% random error is estimated in GEOS-FP U_{10} data, which is consistent with the $\sim$1.5 m/s error standard deviation in wind speed assumed by Varon et al. (2020a). A random distribution of U_{10} values is generated and converted into a distribution of Q values using Eqs. 3-4 and the actual values of IME and L. This U_{10} error contribution is combined quadratically with that from the standard error of the IME to generate the final Q random error. The consideration of systematic errors in Q such as from intrinsic structural errors of the IME model are considered to be out of the scope of this work.

2.5. *End-to-end simulations*

We have investigated the performance of PRISMA for methane retrieval using end-to-end simulations. Full PRISMA scenes are simulated because the spatial context conditions the performance of data-driven methods such as the matched-filter.

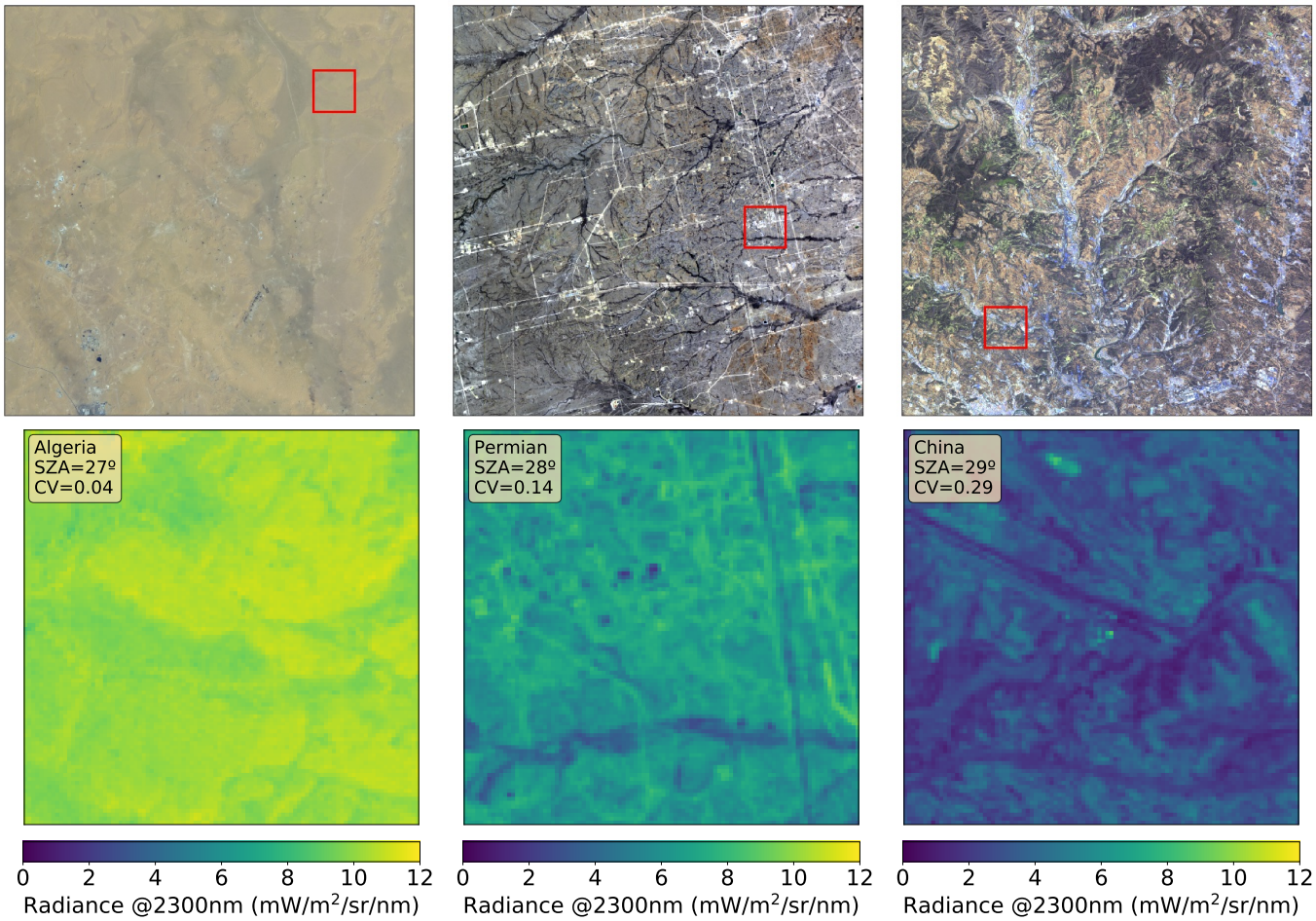

Fig. 3. Input data for the end-to-end simulations in this work. Top row, true color composites of the three PRISMA images (1000×1000 pixels) used as input for the sensitivity analysis. The red squares depicts the location of the 100×100 pixels subsets where simulated methane plumes are included. Bottom row, maps of top-of-atmosphere radiance at 2300 nm for the 100×100 subsets in the red squares of the top row. CV in the label on the top left corner of each panel refers to the coefficient of variation (standard deviation over mean) of radiance at 2300 nm within the image, and SZA to the sun zenith angle.

The most common approach for the forward simulation of TOA imaging spectroscopy images consists in the conversion of "denoised" input surface reflectance spectra into TOA radiance spectra through radiative transfer simulations (e.g. Guanter et al., 2009a; Foote et al., 2020). The resulting high spectral resolution TOA radiance spectra are convoluted with the instrument's spectral response. Noise is finally added using appropriate noise-radiance curves. This type of approach allows to vary the illumination and observation geometries, the atmospheric state and the instrument spectral and radiometric performance. However, it is not feasible for this type of simulation methods to capture the entire spread of environmental effects and instrumental artifacts occurring in real image.

In this work, we use the previous simulation approach to test the impact of the SZA on the retrieval performance (see Sec. 3.1.3), but the core part of the sensitivity analysis relies on a different forward simulation strategy. Similar to Cusworth et al. (2019), we add the effect of simulated methane plumes on top of real PRISMA TOA radiance images without identified plumes. The simulated plumes were generated by large-eddy simulations with the Weather and Research Forecasting Model (WRF-LES) at 30 m×30 m resolution for a mean wind speed of 3.5 m/s (Varon et al., 2018; Cusworth et al., 2019). The 3D volume mixing ratio enhancement (ΔVMR) data generated with the WRF-LES are converted into a two-way spectral atmospheric transmittance using methane absorption cross section data from the HITRAN data base, vertical profiles of the column density of dry air from MERRA-2 meteorological reanalysis, and geometric air mass factors for the actual illumination and observation zenith angles. We choose one of the five time slices provided in the WRF-LES simulations and scale the ΔXCH_4 values from a 100 kg/h simulation to different Q values (500, 1000, and 2000 kg/h). The resulting spatially-distributed high resolution transmittance spectra are convoluted with PRISMA's spectral response and then multiplied by the original PRISMA TOA radiance spectrum. The PRISMA-like TOA radiance spectra are finally corrected for small radiometric offsets due to the multiplication of two spectrally resampled variables (original TOA radiance and the plume transmittance). These operations

are performed on a per-column basis in order to account for across-track variations in spectral calibration. The result of the process is a real PRISMA 1000×1000 pixel TOA radiance image including a simulated methane plume over a selected area.

This process is applied to three different locations in Algeria, USA (Permian Basin) and China (see Fig. 3). These are chosen because of their varying surface brightness and homogeneity, which is the main driver of the methane detection threshold as it will be shown later. The site in Algeria represents the optimal observation conditions with a bright and spatially homogeneous surface, whereas the China site represents the most challenging conditions because of a relatively dark and heterogeneous surface. The similar sun zenith angle (SZA) of the three images (27, 28 and 29°) allows to minimize the effect of SZA variations in the results. The simulated plumes are added in areas inside these images where real plumes have been detected in other data sets. True color composites of these three selected images and maps of the TOA radiance at 2300 nm for 100×100 pixel subsets containing the plume are shown in Fig. 3.

The matched-filter retrieval algorithm is applied to the resulting full images including the simulated plume as it would be done with an original PRISMA image. A 200×200 pixel subset from the ΔXCH_4 map resulting from this end-to-end simulation for the Permian image and a Q=1000 kg/h plume is shown in Fig. 4. The comparison of the two maps shows how the central pixels of the plume with the highest ΔXCH_4 values are well reconstructed in the retrieved map, but also noise and false positives reproducing surface structures are prominent.

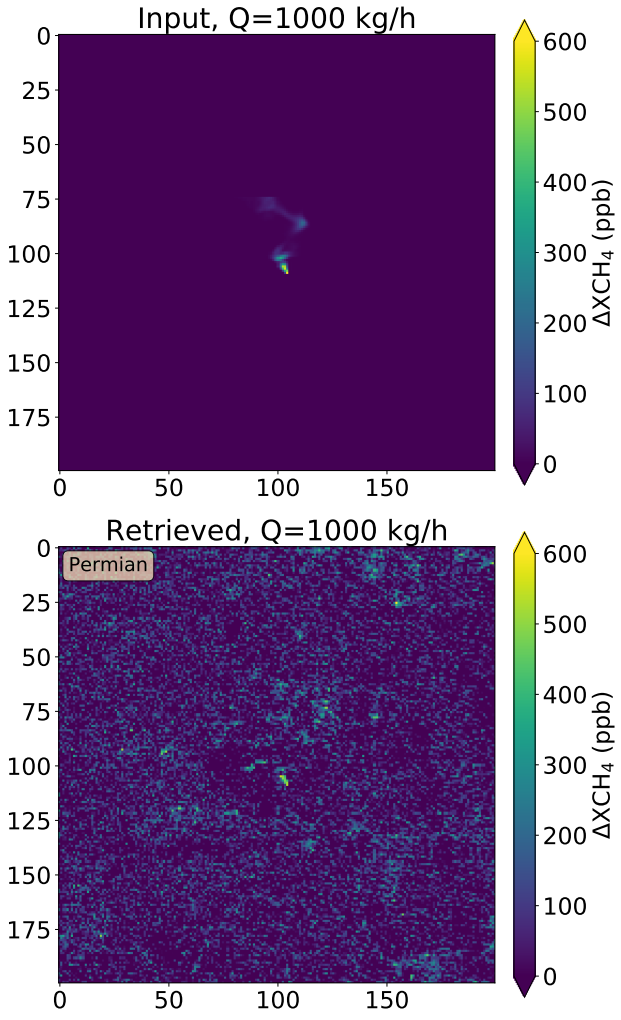

Fig. 4. Comparison of input and retrieved ΔXCH_4 maps for a simulation at the Permian Basin site with an emission flux rate Q of 1000 kg/h.

3. Results

3.1. *Sensitivity analysis based on end-to-end simulations*

3.1.1. *Retrieval performance for different sites*

End-to-end simulation results for the three sites and three Q values (500, 1000, and 2000 kg/h) are displayed in Fig. 5. ΔXCH_4 maps are shown for the 100×100 pixel subsets displayed in Fig. 3. The strong impact of the surface characteristics can be clearly observed. Whereas the 500 kg/h plume would be easily detectable at the Algeria site, at least 1000 kg/h would be needed for a detection in the Permian Basin site, and even higher than 2000 kg/h for the China site. It must be remarked that the noise and retrieval errors in these images are the same ones as in the original PRISMA images used as input for the simulations, as only the plume pixels have been added to the original PRISMA radiance data. The noise in the retrieved ΔXCH_4 maps is therefore linked to the input radiance image and independent of the Q values used in the simulation. By noise we mean here both the random measurement noise (typically dominated by multiplicative shot-noise) propagated to ΔXCH_4 by the retrieval, and spatially-coherent retrieval errors which are caused by surface structures with absorption features in the SWIR bands used for methane retrieval (Ayasse et al., 2018).

The range of detection limits that we are estimating from the visual inspection of our end-to-end simulation results in Fig. 5 is supported by simple mass-balance calculations. For example, if we take the "minimum source" relationship provided in Jacob et al. (2016), a retrieval precision of 61 ppb (3.3% if we assume a 1850 ppb methane background concentration) such as in the case of the Algeria site would lead to a detection limit between 370 and 900 kg/h for a wind speed between 2 and 5 m/s (630 kg/h for the 3.5 m/s wind speed used as input in our plume simulations).

We analyze the distribution of retrieval errors for the three sites using the original images (no-plume case). The histograms generated from the resulting 100×100 ΔXCH_4 subsets are shown in Fig. 6. It can be seen that errors tend to follow a Gaussian distribution, likely because the contribution of random instrumental noise dominates with respect to the limited number of spatially-coherent retrieval

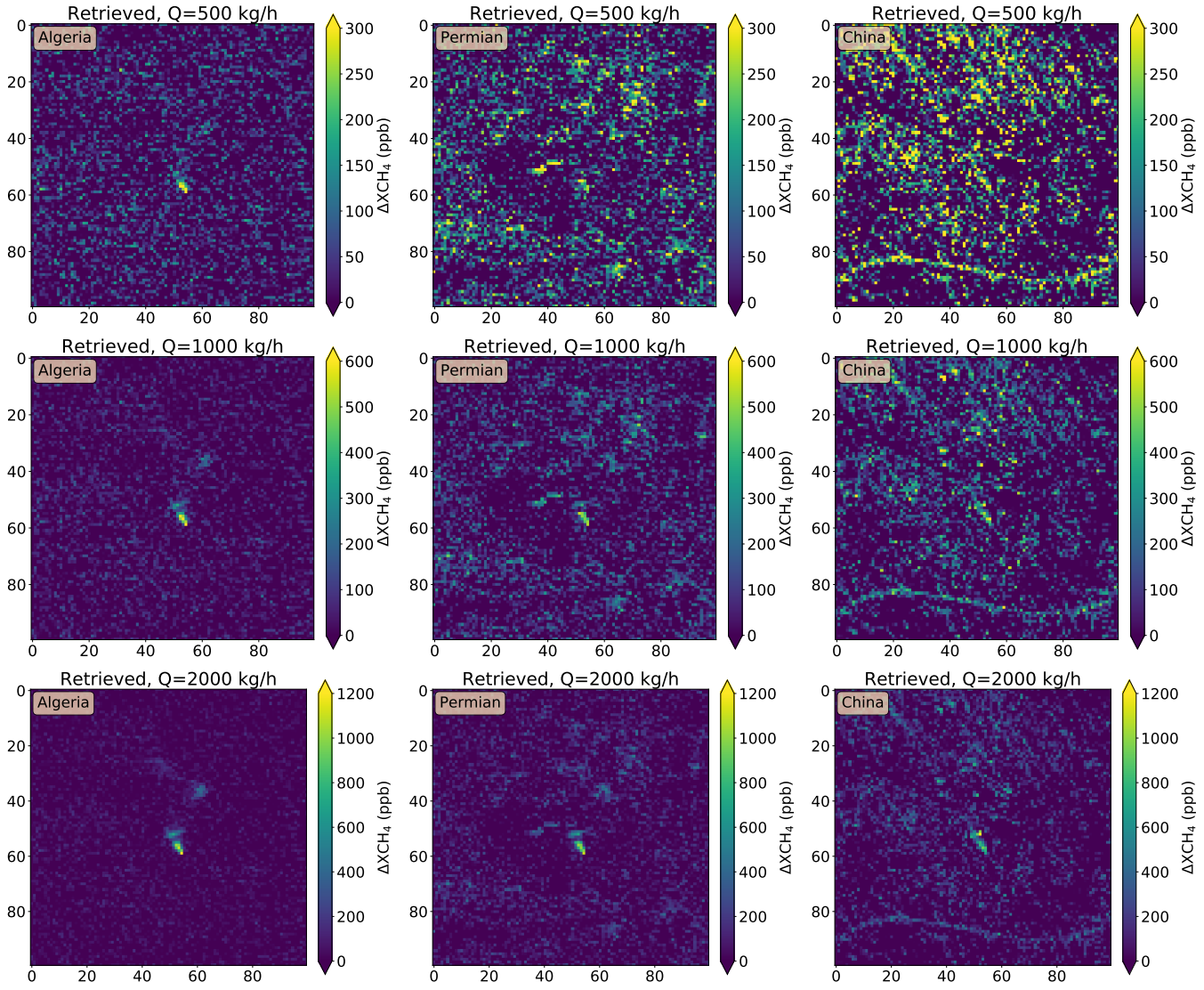

Fig. 5. Maps of retrieved ΔXCH_4 from the simulations at the three sites and for three values of the emission flux rate Q.

artifacts. The σ values provided in the figure depict the standard deviation of ΔXCH_4 in the 100×100 pixel subsets and are hence a good estimation of the retrieval precision error for the three sites. These values show that the retrieval precision error is more than three times higher for the China site (197 ppb) than for the Algeria site (61 ppb). A relatively large negative bias of 29 ppb is also found for the China site. This again indicates the very strong dependence of the retrieval error and subsequent plume detection limit on the surface type.

A more quantitative representation of the retrieval performance is provided in Fig 7. It compares the input and the retrieved ΔXCH_4 for the same 100×100 pixel subsets and the 1000 and 2000 kg/h sources plotted in Fig. 5. As expected, the retrieval performs best for the Algeria case, with a substantial number of pixels above the noise level already for the Q =1000 kg/h source, whereas a higher scattering is found for the Permian and the China sites. The highest ΔXCH_4 values appear to be underestimated by the retrieval at the China site. The Permian site is the one for which the root mean square error (RMSE) is the most different to the σ values shown in Fig. 6 (128 and 119 ppb, respectively), which would suggest that there is a higher fraction of plume pixels in this site where the residuals between the input and retrieved ΔXCH_4 values deviate from a normal distribution.

We have used our end-to-end simulations to test the implications of these findings for the detection of methane plumes and the estimation of Q with the IME-based model described in Section 2.4. Similar to Thompson et al. (2016), we have investigated the number of statistically-significant pixels in the output ΔXCH_4 maps by comparing the ΔXCH_4 values with the noise level. In particular, we consider as statistically-significant the ΔXCH_4 values which are twice higher than the noise level (2σ threshold, p <0.05). In addition, using the same end-to-end simulation results, we have investigated the fraction of the total IME that we are able to reconstruct from ΔXCH_4 maps

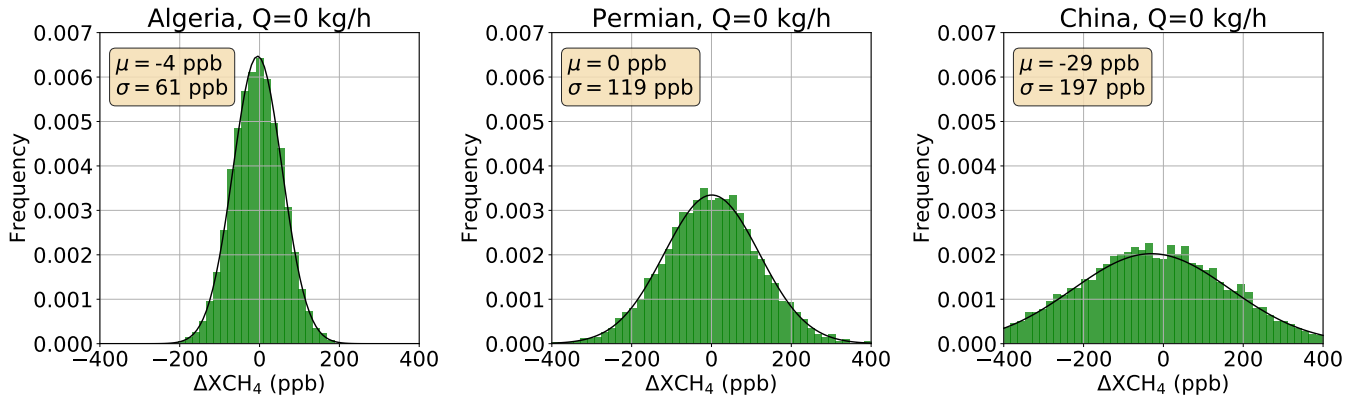

Fig. 6. Histograms of the retrieved ΔXCH_4 inside the selected 100×100 subset areas of the three sites for the no-plume case. The μ and σ values in the box represent the mean and standard deviation of the distributions, respectively.

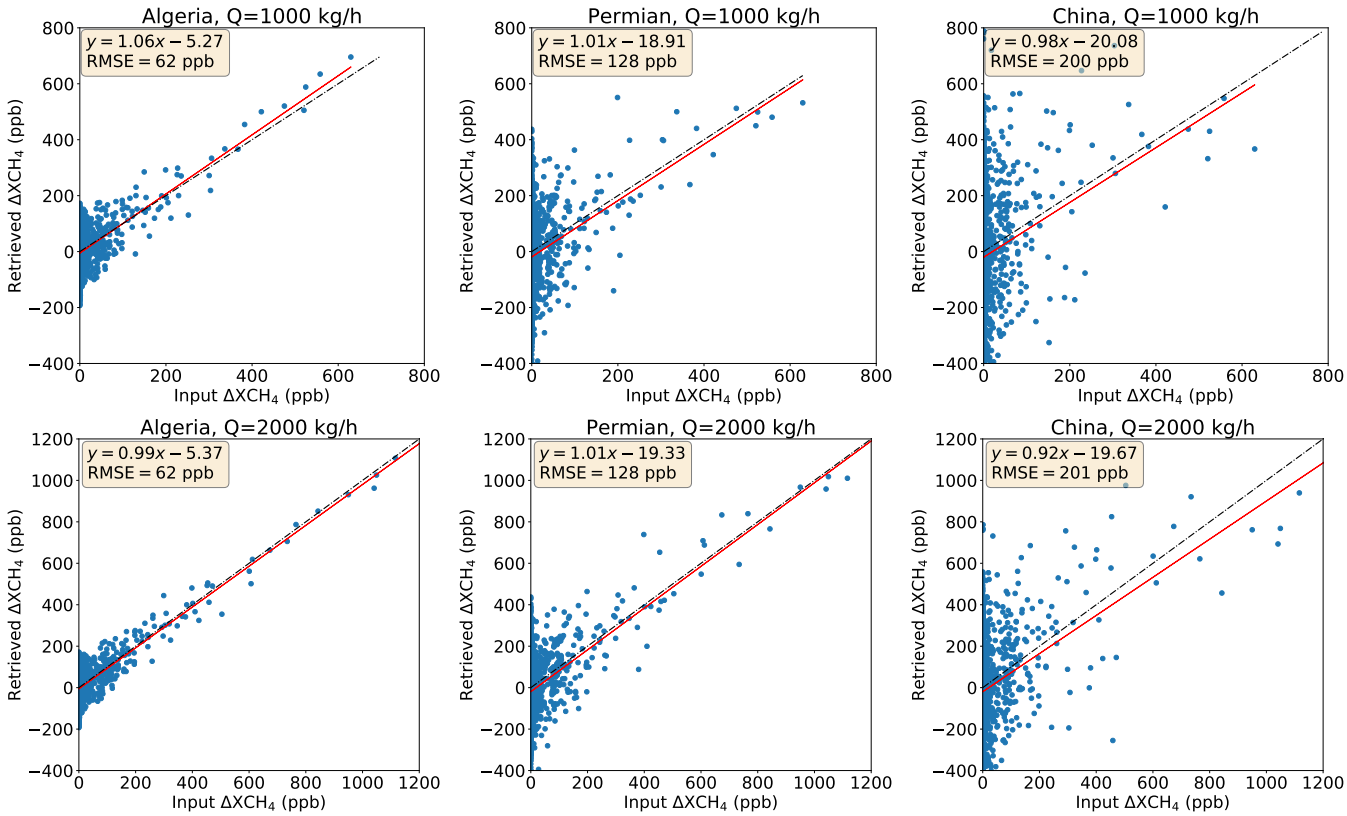

Fig. 7. Scatter plots of the input and retrieved ΔXCH_4 for the simulations at the three sites and emission flux rates Q of 1000 and 2000 kg/h.

considering only pixels with ΔXCH_4 values above the noise level. In this case, we take a 1σ threshold to separate plume pixels from background noise, as we assume that spatial aggregations of pixels above the 1σ level would in practice be identified as plume pixels by the visual inspection process described in Sec. 2.3.

The results of these two exercises are plotted in Fig. 8. As expected, the number of significant retrievals inside the plume and the fraction of the input IME that we can reconstruct follow similar trends. Both increase with the intensity of the source, and both are highest for the Algeria site, followed by the Permian site and the China site. The number of significant plume pixels in Algeria is about twice higher than for the other two sites. It is interesting to note that pixels contributing to an important fraction of the IME are not captured in the retrieved ΔXCH_4 maps. Even for the relatively strong 2000 kg/h plume, the missing fractions of the total IME are about 20% for the Algeria site, about 40% for the Permian site, and 50% for the China site. These fractions become even larger for smaller Q values, and the same if we set a more strict plume mask threshold (e.g. 2σ, to retain p <0.05 statistically-significant pixels). However, it is difficult to provide a more robust estimate of the fraction of IME missing in the retrieved ΔXCH_4 maps because our plume mask identification relies on a subjective approach without any particular threshold value to sepa-

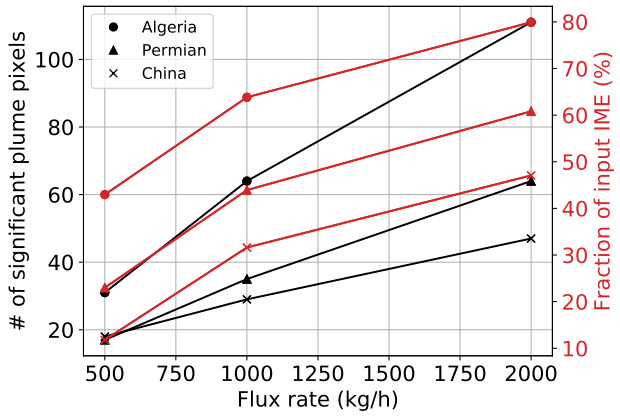

Fig. 8. Test of methane detection limits. The black lines (left y-axis) show the number of pixels in the input plume for which the retrieved ΔXCH_4 values are statistically-significant (p <0.05). The red lines (right y-axis) depict the fraction of the IME of the input plume which can be reconstructed with the retrieved ΔXCH_4 values.

rate plume pixels from the background. A complete analysis of the impact of retrieval noise on the estimation of Q would also require to consider the effect of retrieval precision on the estimation of the L parameter (which has an opposite impact on Q than the IME), and on the U_{10}-U_{eff} conversion curves, in which precision errors are taken into account. We consider such analysis to be out of the scope of the present work.

3.1.2. *Sensitivity of the retrieval to errors in spectral calibration*

We have evaluated the impact of spectral calibration errors on ΔXCH_4 retrievals. For this, we have first checked the accuracy of the spectral calibration information attached to the PRISMA data using the scene-based spectral characterization method described in Sec. 2.2, and then we have simulated the effect of deviations from the nominal calibration on ΔXCH_4 maps.

The results obtained for the Algeria scene displayed in Fig. 3 are shown in Fig. 9. The across-track variation of the estimated center wavelength follows the linear same trend as the one in the nominal calibration (decrease from the left to the right hand side of the image), although the estimated curve has a lower slope than the nominal one. This results in peak deviations in center wavelength of ∼-1.5 nm at the left edge of the image and ∼0.5 nm at the right edge. Regarding the bandwidth (represented by the FWHM of a Gaussian spectral response function), nominal and estimated curves follow opposite trends, the nominal FWHM increasing almost linearly from left to right, and the estimated one decreasing from left to right in a non-linear fashion. The reasons for this discrepancy are not yet clear. We find that the same across-track trends repeat for all images processed for this work, although the absolute values of the detected spectral shift and FWHM changes vary from one data set to another, with maximum differences of ∼1.0 nm for the center wavelength (0.3 nm standard deviation) and

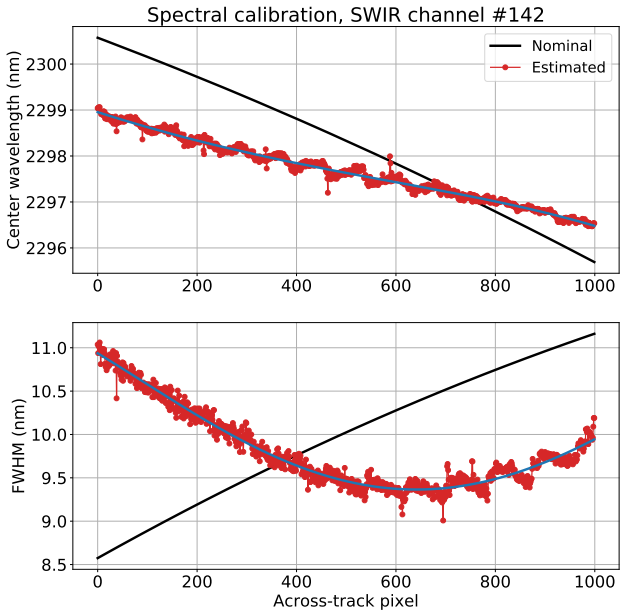

Fig. 9. Example of across-track variation in channel center wavelength and width (full-width at half-maximum, FWHM) for a spectral channel around 2300 nm and the Algeria image shown in Fig. 3a, according to the nominal spectral calibration and the updated calibration based on the data. .

∼3.0 nm for the FWHM (1.4 nm standard deviation).

We acknowledge that those differences in the results obtained for different images can be partly attributed to systematic errors in the spectral characterization method, for example from uncertainties in the atmospheric composition (e.g. water vapor concentration) which would especially affect the estimation of the FWHM. Nevertheless, the across-track trends for both channel position and width are robust across images. It must also be noted that our spectral characterization method assumes Gaussian spectral response functions, so the estimated center and width must be understood as effective parameters linked to the Gaussian shape approximation. In any case, the update of the spectral calibration parameters improves our ability to model the TOA radiance spectrum (see Fig. 10), which justifies the application of this spectral characterization process to each PRISMA data set prior to the ΔXCH_4 retrieval.

The impact of potential spectral calibration errors on ΔXCH_4 retrievals from PRISMA is illustrated in Fig. 11. It shows the difference in retrieved ΔXCH_4 maps when errors in spectral calibration are added. The Permian Basin site with a source of 2000 kg/h are chosen as a reference, and the errors in channel center wavelength and FWHM are taken from those at the edges of the across-track direction shown in Fig. 9. Interestingly, the two sets of spectral calibration errors (-1.5 nm in center wavelength and +2.5 nm in FWHM in one case, +0.5 nm in center wavelength and -1.5 nm in FWHM in the other) have a very different impact on the ΔXCH_4 retrievals. In the first case, the differences between the two ΔXCH_4 outputs seem to be spatially uncorrelated, whereas in the second case the difference mostly leads to a systematic change in the plume

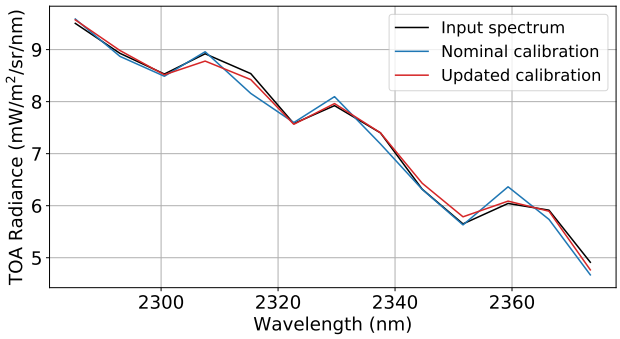

Fig. 10. Example of spectral re-calibration for a top-of-atmosphere radiance spectrum calculated as the average of all along-track spectra in the column 3 of the Algeria image shown in Fig. 3a. The input spectrum is compared with modelled spectra using the nominal and updated spectral configuration (channel center wavelength and width).

ΔXCH_4 values, which would lead to an error in the plume IME of about 10%. We interpret that this impact of the sign of spectral calibration errors on the retrieved ΔXCH_4 values is related to the non-symmetric spectral structure of the methane absorption in the 2110–2450 nm fitting window (see Fig. 2), and also to the fact that spectral shifts and changes in FWHM may introduce different effects (e.g. errors in FWHM appear as systematic errors in ΔXCH_4). Similar results have been found for the other two sites in the sensitivity analysis.

3.1.3. *Sensitivity of the retrieval to the illumination angle*

We have assessed how illumination conditions affect the retrieval in the last part of the sensitivity analysis. This can be due, for example, to the dependence of measurement noise on the incoming radiance level through the shot-noise component, or to a different sensitivity of the signal to methane concentration enhancements when modifying the atmospheric path length.

For this exercise, we have simulated PRISMA-like images for different SZAs by performing a complete forward simulation. The Permian site is again taken as a reference. Atmospheric radiative transfer simulations are used to convert input denoised surface reflectance spectra into TOA radiance, and measurement noise is added using existing noise-radiance curves (see Sec. 2.5). No plume is included in this simulation, as the goal is only to evaluate how retrieval precision errors vary with SZA.

The histograms generated from the ΔXCH_4 maps resulting from the matched-filter processing of these simulations are shown in Fig. 12. It can be seen that retrieval errors decrease for the lower SZAs, which can be explained by the improvement in the measurement SNR. The range of variation in ΔXCH_4 between the extreme 20 and 60° SZAs is 25 ppb (∼20%) which represents a smaller impact than that of the surface characteristics evaluated in Sec. 3.1.1. It must also be considered that we are assuming a flat surface; over rugged terrain, there would be at-surface illumination effects from topography which would add extra variability in ΔXCH_4.

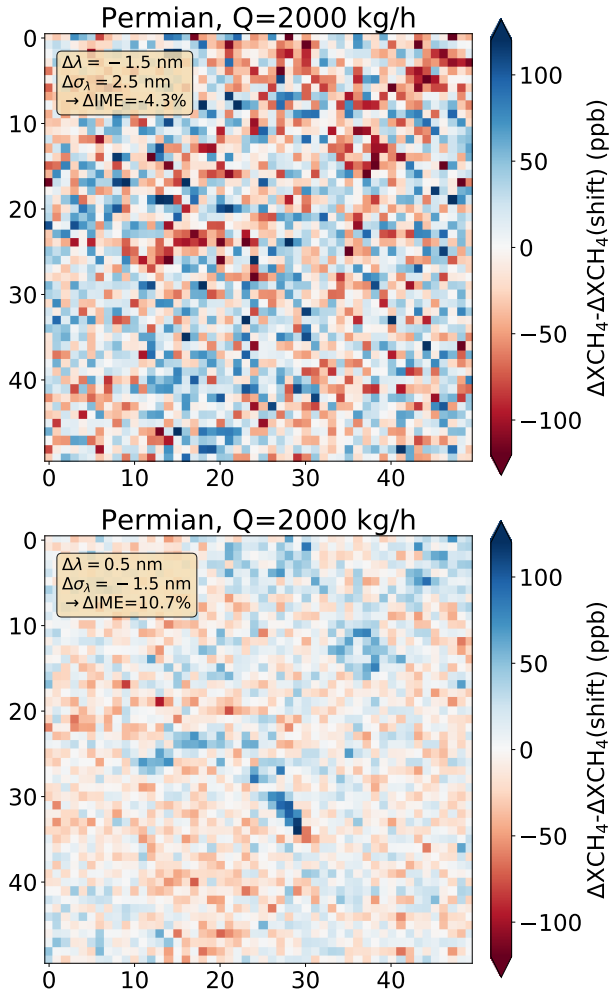

Fig. 11. Changes in ΔXCH_4 and integrated mass enhancement (IME) from errors in the knowledge of the channel center wavelength ($\Delta\lambda$) and FWHM ($\Delta\sigma_\lambda$). Simulations are performed for the Permian Basin site and a flux rate Q of 2000 kg/h. The selected values correspond to the left edge of the detector array in the case of the top panel, and to the right edge in the case of bottom panel (see Fig. 9).

3.2. *Results from real data*

Examples of methane ΔXCH_4 maps derived from real PRISMA images over different sites are shown in Fig. 13. In addition to the simple matched-filter implementation which has been used along this study so far, we have also generated ΔXCH_4 maps with the advanced MAG1C matched-filter retrieval described in Sec. 2.1. All the maps correspond to 150×150 pixel subsets. The first column shows two plumes detected in an oil and gas extraction field in Algeria; the second column shows two large plumes from close sources in oil fields of Turkmenistan; the third row shows a small plume from a well pad in the Permian Basin, and the forth column represents a large emission from a coal mine in the Shanxi region in China.

Consistently with the previous simulation-based sensitiv-

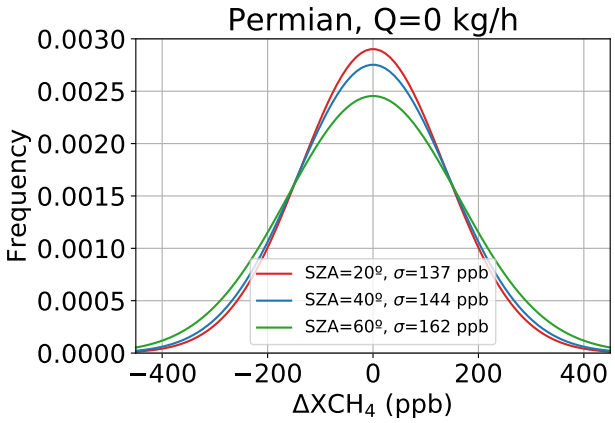

Fig. 12. Histograms of the retrieved ΔXCH_4 in the Permian Basin for the no-plume case and three different sun zenith angle (SZA) values.

ity analysis, clean plumes can be observed at the bright and homogeneous sites in Algeria and Turkmenistan, whereas different surface elements (roads, buildings, well pads, ...) are clearly observable at the Permian and China sites. For this particular set of examples, the results from the Permian image are particularly bad, due to the large number of false methane enhancements happening due to the confusion of the retrieval with surface structures and the relatively low ΔXCH_4 values of the plume. Surface features are also present in the ΔXCH_4 map from the Shanxi region in China, but in this case the higher concentrations and the greater spatial extent of the plume make these false enhancements to be less prominent than in the Permian Basin example.

With respect to the comparison between the simple and advanced matched-filter implementations, slightly higher ΔXCH_4 values are found for MAG1C (third row of Fig. 13), for which ppb values are calculated from its ppm·m output with a 0.125 conversion factor (Thompson et al., 2016). The comparison of the results from the two retrievals confirms the expected lower sensitivity of MAG1C to measurement noise thanks to the sparsity assumption. The sensitivity to surface structures, however, seems to be similar for the two methods, despite the "albedo correction" implemented in MAG1C. This suggests that the sensitivity of the retrieval to surface patterns is caused by absorption features in the surface elements spectrally overlapping the methane band at 2300 nm, rather than to changes in the overall brightness of the surface (Ayasse et al., 2018). On the other hand, plumes appear to be smaller in the MAG1C maps, which could imply that a fraction of the plume tails are considered as noise by MAG1C. This could low-bias the IME estimates by MAG1C with respect to the ones by the basic matched-filter as discussed in Sec. 3.1.1.

Final results from our processing of real PRISMA data are shown in Fig. 14. The maps have been geometrically-corrected, the plumes have been extracted from the background and represented on top of high-resolution true color images. The Q values estimated with the IME-based method described in Sec. 2.4 are shown for all plumes. Q values range between the 1,700±600 kg/h calculated for the smaller plume in the Permian and the 35,500±12,000 kg/h massive double-plume in Turkmenistan, both of them also shown in "raw" format in Fig. 13.

4. Summary and Outlook

In this study we have investigated the potential of the PRISMA satellite imaging spectroscopy mission to map strong methane plumes, such as the ones typically originating from oil and gas production activities or coal mining. Our analysis has included a simulation-based sensitivity analysis and the evaluation of a number of real PRISMA images. In both cases, the retrieval of methane concentration enhancements (ΔXCH_4) has relied on the data-driven matched-filter method. We have applied this type of retrieval because of its high computational efficiency and because DOAS-like physically-based methods cannot properly account for uncertainties in PRISMA's radiometric and spectral responses as data-driven methods do.

Our simulation-based sensitivity analysis has evaluated the capability of PRISMA to detect and quantify methane emissions at three different surface types, ranging from ideal conditions for methane mapping (bright and spatially homogeneous area in Algeria) to challenging ones (relatively dark and heterogeneous surfaces in the Permian Basin and the Shanxi coal mining region in China). The results from this analysis confirm the strong dependence of the ΔXCH_4 retrieval performance on the surface type. Retrieval 1-σ precision errors (accounting for both instrumental noise and surface variability) range from ∼60 ppb in the Algeria image to ∼200 ppb in the China case. The visual evaluation of the retrieved ΔXCH_4 maps shows that plumes with Q below 500 kg/h can be easily detected in Algeria, whereas values close to 2,000 kg/h are needed for plume detection over the China site.

We have also observed a strong dependence of the IME, an input for flux rate calculations in our processing chain, on the site characteristics and the Q itself. Large fractions of the true plume might not be captured in PRISMA-derived ΔXCH_4 maps, especially for the smaller plumes, which might result in important underestimations of the IME. For the quantification of the impact that retrieval noise might have on IME-based Q estimates, also the impact of noise on the estimation of the L parameter in the IME model and the ability of the empirical U_{10}-U_{eff} curves to account for retrieval noise should be investigated.

The sensitivity analysis has been complemented with two further tests, which have shown a peak ΔXCH_4 systematic error of about 10% from uncertainties in PRISMA's spectral calibration, and a 20% variation in the retrieval precision from a SZA of 20° to 60° over a Permian Basin area.

The results from this sensitivity analysis help to understand the role of different factors on the retrieval performance. However, we acknowledge that simulations over a broader range of conditions, especially regarding surface ar-

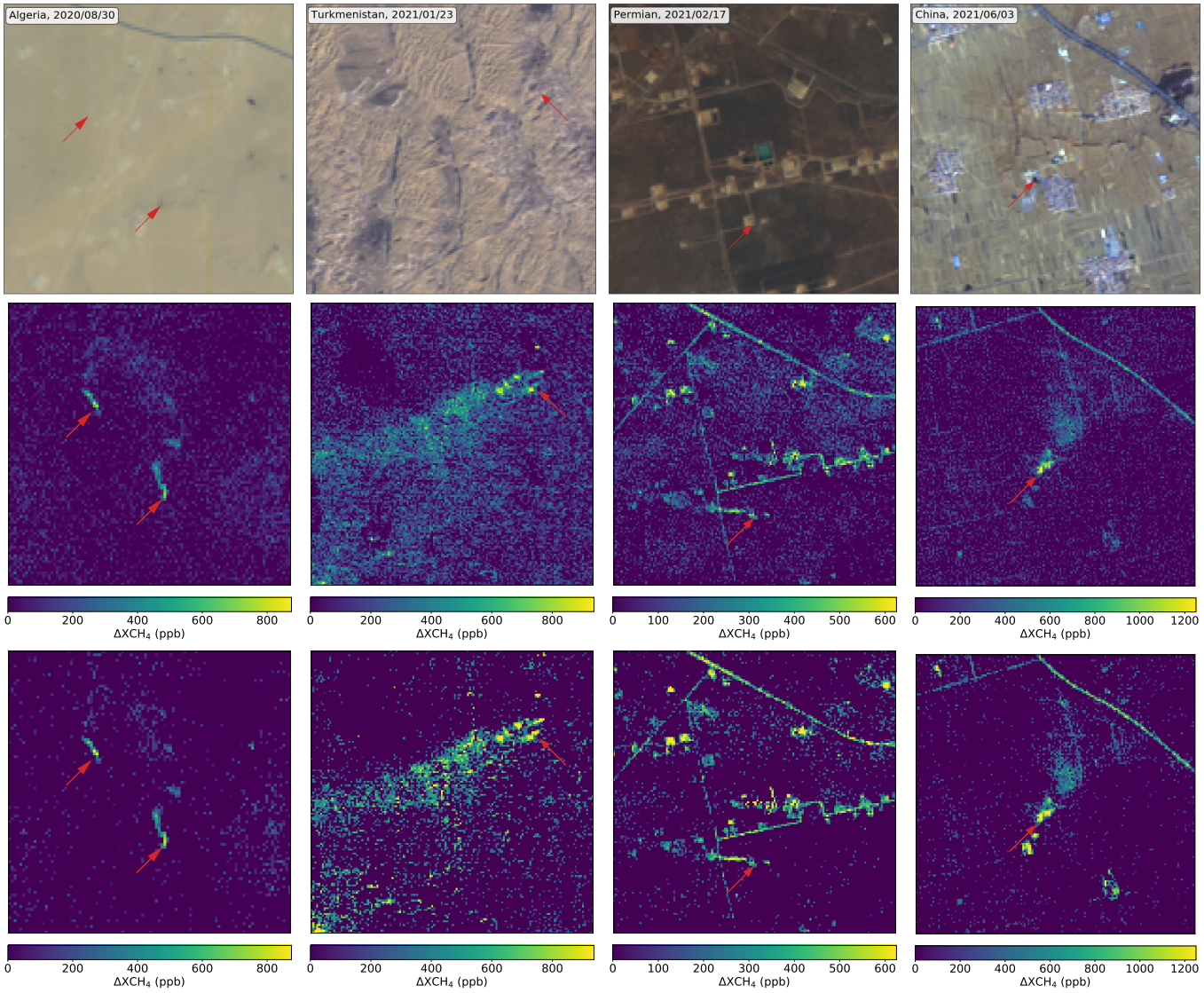

Fig. 13. Sample true color composites (first row) and ΔXCH_4 maps produced from real PRISMA data at different sites with the basic matched-filter retrieval (second row) and the MAG1C code (third row). Red arrows show the origin of the plume in both true color composites and ΔXCH_4 maps.

eas and plume strength and morphology, would be needed to produce robust error budgets for ΔXCH_4 retrieval and subsequent Q estimation, and also for a quantitative definition of detection limits for different areas.

Results from real data have confirmed the strong dependency of the retrieval on the surface type. Whereas plumes are easily detectable over bright and homogeneous surfaces in Algeria and Turkmenistan oil and gas extraction fields, the detection of plumes at the Permian Basin and China's Shanxi region requires a very careful visual inspection because of the strong impact of surface structures in the latter cases. The reduction of the high number of false positives in ΔXCH_4 maps is critical for the broad application of PRISMA data for methane mapping. Most of those false positives are due to the spectral overlap of surface absorption features with the 2300 nm methane absorption used for the retrieval. Retrieval approaches exploiting spectral information from other parts of the broad spectrum window sampled by PRISMA, for example from the weaker methane absorption at 1700 nm, could help reduce the impact of the background surface. This would lead to lower plume detection limits, and it would enable the development of automatic plume detection procedures to avoid time-consuming and error-prone procedures based on visual inspection.

Our results show that PRISMA can play an important role in the ongoing international effort to detect methane point emissions from fossil fuel production activities, especially in the case of oil and gas extraction basins with bright and homogeneous surfaces. Furthermore, PRISMA is a precursor to a number of upcoming spaceborne imaging spectroscopy missions with potential for methane mapping. This includes the German EnMAP mission (Guanter et al., 2015), with similar characteristics to PRISMA and launch

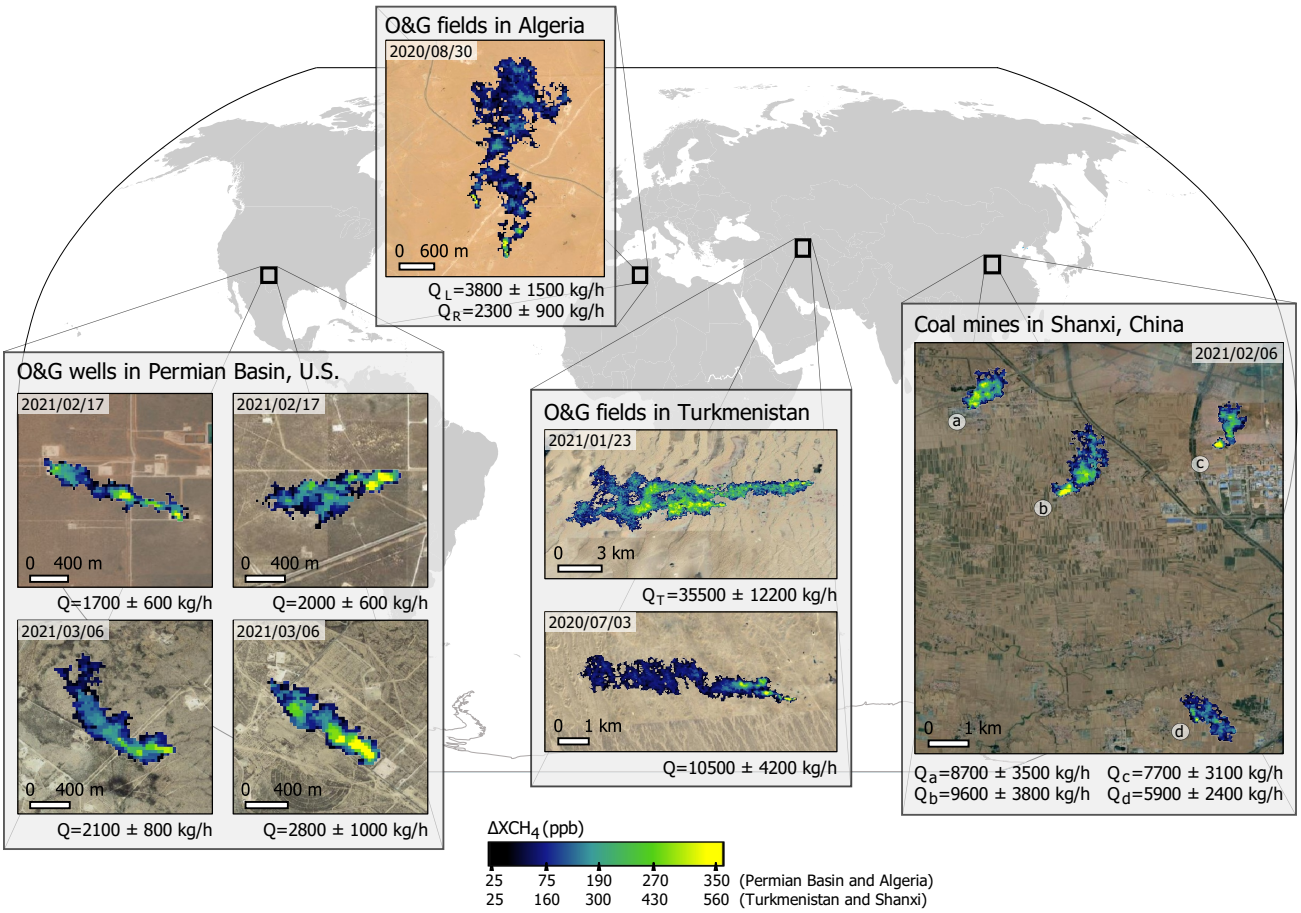

Fig. 14. ΔXCH_4 maps from plumes detected in real PRISMA images acquired in four different parts of the world (oil and gas extraction fields in Algeria, Turkmenistan, and the Permian Basin (USA), and coal mines in the Shanxi region in China). The Algeria panel shows two plumes in close proximity; Q_L refers to the emission flux of the plume on the left and Q_R to the one of the right. There are also two plumes in the top sub-panel of the Turkmenistan panel, where Q_T corresponds to the total flux emitted by the two. The ranges of the color scale differ for either Permian and Algeria or Turkmenistan and Shanxi region.

expected for 2022; Carbon Mapper (Carbon Mapper Inc., 2021), which is a joint effort of public and private entities in the U.S. to implement by 2023 a constellation of imaging spectrometers optimized for methane and CO_2 mapping; and the CHIME and SBG missions (Copernicus/EU/ESA and NASA, respectively), which would provide hyperspectral data with global coverage every 2–3 weeks each. This set of imaging spectroscopy missions will complete an exciting remote sensing scenario for high resolution methane mapping, which will include the GHGSat constellation, the MethaneSAT mission (Environmental Defense Fund, 2021) and a series of multispectral systems (Sentinel-2, Landsat, WorldView3) with a poorer sensitivity to methane but able to produce dense time-series of emissions over bright and homogeneous areas (Varon et al., 2020b). The joint exploitation of all these missions promises a breakthrough in the mitigation of unintended methane emissions from industrial activities in the next years.

Acknowledgment

The authors would like to thank the Italian Space Agency, and in particular Ettore Lopinto (Mission Director), for the PRISMA data used in this work. Markus Foote (University of Utah) is also thanked for making the MAG1C code available to the scientific community. Javier Gorroño is funded by the ESA Living Planet Fellowship.

References

Ayasse, A. K., Dennison, P. E., Foote, M., Thorpe, A. K., Joshi, S., Green, R. O., Duren, R. M., Thompson, D. R., Roberts, D. A., 2019. Methane mapping with future satellite imaging spectrometers. Remote Sensing 11 (24). URL https://www.mdpi.com/2072-4292/11/24/3054

Ayasse, A. K., Thorpe, A. K., Roberts, D. A., Funk, C. C., Dennison, P. E., Frankenberg, C., Steffke, A., Aubrey, A. D., 2018. Evaluating the effects of surface properties on methane retrievals using a synthetic airborne visible/infrared imaging spectrometer next generation

(aviris-ng) image. Remote Sensing of Environment 215, 386 – 397.
URL http://www.sciencedirect.com/science/article/pii/S0034425718302967

Barré, J., Aben, I., Agustí-Panareda, A., Balsamo, G., Bousserez, N., Dueben, P., Engelen, R., Inness, A., Lorente, A., McNorton, J., Peuch, V.-H., Radnoti, G., Ribas, R., 2020. Systematic detection of local ch_4 emissions anomalies combining satellite measurements and high-resolution forecasts. Atmospheric Chemistry and Physics Discussions 2020, 1–25.
URL https://acp.copernicus.org/preprints/acp-2020-550/

Borchardt, J., Gerilowski, K., Krautwurst, S., Bovensmann, H., Thorpe, A. K., Thompson, D. R., Frankenberg, C., Miller, C. E., Duren, R. M., Burrows, J. P., 2020. Detection and quantification of ch_4 plumes using the wfm-doas retrieval on aviris-ng hyperspectral data. Atmospheric Measurement Techniques Discussions 2020, 1–34.
URL https://amt.copernicus.org/preprints/amt-2020-275/

Brazile, J., Neville, R. A., Staenz, K., Schläpfer, D., Sun, L., Itten, K. I., 2008. Toward scene-based retrieval of spectral response functions for hyperspectral imagers using fraunhofer features. Canadian Journal of Remote Sensing 34 (sup1), S43–S58.
URL https://doi.org/10.5589/m07-069

Carbon Mapper Inc., 2021. Carbon Mapper. https://carbonmapper.org/.

Cogliati et al., 2021. The PRISMA imaging spectroscopy mission: overview and first performance analysis. Remote Sensing of EnvironmentIn press.

Cusworth, D. H., Duren, R. M., Thorpe, A. K., Pandey, S., Maasakkers, J. D., Aben, I., Jervis, D., Varon, D. J., Jacob, D. J., Randles, C. A., Gautam, R., Omara, M., Schade, G. W., Dennison, P. E., Frankenberg, C., Gordon, D., Lopinto, E., Miller, C. E., 2021. Multisatellite imaging of a gas well blowout enables quantification of total methane emissions. Geophysical Research Letters 48 (2), e2020GL090864, e2020GL090864 2020GL090864.
URL https://agupubs.onlinelibrary.wiley.com/doi/abs/10.1029/2020GL090864

Cusworth, D. H., Duren, R. M., Thorpe, A. K., Tseng, E., Thompson, D., Guha, A., Newman, S., Foster, K. T., Miller, C. E., may 2020. Using remote sensing to detect, validate, and quantify methane emissions from california solid waste operations. Environmental Research Letters 15 (5), 054012.
URL https://doi.org/10.1088/1748-9326/ab7b99

Cusworth, D. H., Jacob, D. J., Sheng, J.-X., Benmergui, J., Turner, A. J., Brandman, J., White, L., Randles, C. A., 2018. Detecting high-emitting methane sources in oil/gas fields using satellite observations. Atmospheric Chemistry and Physics 18 (23), 16885–16896.
URL https://acp.copernicus.org/articles/18/16885/2018/

Cusworth, D. H., Jacob, D. J., Varon, D. J., Chan Miller, C., Liu, X., Chance, K., Thorpe, A. K., Duren, R. M., Miller, C. E., Thompson, D. R., Frankenberg, C., Guanter, L., Randles, C. A., 2019. Potential of next-generation imaging spectrometers to detect and quantify methane point sources from space. Atmospheric Measurement Techniques 12 (10), 5655–5668.
URL https://amt.copernicus.org/articles/12/5655/2019/

de Gouw, J., Veefkind, J., Roosenbrand, E., Dix, B., Lin, J., Landgraf, J., Levelt, P., 12 2020. Daily satellite observations of methane from oil and gas production regions in the united states. Scientific Reports 10.

Duren, R., Thorpe, A., Foster, K., Rafiq, T., Hopkins, F., Yadav, V., Bue, B., Thompson, D., Conley, S., Colombi, N., Frankenberg, C., McCubbin, I., Eastwood, M., Falk, M., Herner, J., Croes, B., Green, R., Miller, C., 11 2019. California's methane super-emitters. Nature 575, 180–184.

Environmental Defense Fund, 2021. MethaneSAT. https://www.methanesat.org/.

Foote, M. D., Dennison, P. E., Thorpe, A. K., Thompson, D. R., Jongaramrungruang, S., Frankenberg, C., Joshi, S. C., 2020. Fast and accurate retrieval of methane concentration from imaging spectrometer data using sparsity prior. IEEE Transactions on Geoscience and Remote Sensing 58 (9), 6480–6492.

Frankenberg, C., Thorpe, A. K., Thompson, D. R., Hulley, G., Kort, E. A., Vance, N., Borchardt, J., Krings, T., Gerilowski, K., Sweeney, C., Conley, S., Bue, B. D., Aubrey, A. D., Hook, S., Green, R. O., 2016. Airborne methane remote measurements reveal heavy-tail flux distribution in four corners region. Proceedings of the National Academy of Sciences 113 (35), 9734–9739.
URL https://www.pnas.org/content/113/35/9734

Gao, B.-C., Montes, M. J., Davis, C. O., 2004. Refinement of wavelength calibrations of hyperspectral imaging data using a spectrum-matching technique. Remote Sensing of Environment 90 (4), 424–433.
URL https://www.sciencedirect.com/science/article/pii/S0034425703002530

Green, R., Pavri, B., Chrien, T., 2003. On-orbit radiometric and spectral calibration characteristics of eo-1 hyperion derived with an underflight of aviris and in situ measurements at salar de arizaro, argentina. IEEE Transactions on Geoscience and Remote Sensing 41 (6), 1194–1203.

Green, R. O., Feb 1998. Spectral calibration requirement for earth-looking imaging spectrometers in the solar-reflected spectrum. Appl. Opt. 37 (4), 683–690.
URL http://ao.osa.org/abstract.cfm?URI=ao-37-4-683

Guanter, L., Kaufmann, H., Segl, K., Foerster, S., Rogass, C., Chabrillat, S., Kuester, T., Hollstein, A., Rossner, G., Chlebek, C., et al., Jul 2015. The EnMAP Spaceborne Imaging Spectroscopy Mission for Earth Observation. Remote Sensing 7 (7), 8830–8857.
URL http://dx.doi.org/10.3390/rs70708830

Guanter, L., Richter, R., Moreno, J., Apr 2006. Spectral calibration of hyperspectral imagery using atmospheric absorption features. Appl. Opt. 45 (10), 2360–2370.
URL http://ao.osa.org/abstract.cfm?URI=ao-45-10-2360

Guanter, L., Segl, K., Kaufmann, H., 2009a. Simulation of optical remote-sensing scenes with application to the enmap hyperspectral mission. IEEE Transactions on Geoscience and Remote Sensing 47 (7), 2340–2351.

Guanter, L., Segl, K., Sang, B., Alonso, L., Kaufmann, H., Moreno, J., Jul 2009b. Scene-based spectral calibration assessment of high spectral resolution imaging spectrometers. Opt. Express 17 (14), 11594–11606.
URL http://www.opticsexpress.org/abstract.cfm?URI=oe-17-14-11594

Irakulis-Loitxate et al., 2021. Satellite-based Survey of Extreme Methane Emissions in the Permian BasinIn press.

Jacob, D. J., Turner, A. J., Maasakkers, J. D., Sheng, J., Sun, K., Liu, X., Chance, K., Aben, I., McKeever, J., Frankenberg, C., 2016. Satellite observations of atmospheric methane and their value for quantifying methane emissions. Atmospheric Chemistry and Physics 16 (22), 14371–14396.
URL https://acp.copernicus.org/articles/16/14371/2016/

Jervis, D., McKeever, J., Durak, B. O. A., Sloan, J. J., Gains, D., Varon, D. J., Ramier, A., Strupler, M., Tarrant, E., 2021. The ghgsat-d imaging spectrometer. Atmospheric Measurement Techniques 14 (3), 2127–2140.
URL https://amt.copernicus.org/articles/14/2127/2021/

Lyon, D. R., Alvarez, R. A., Zavala-Araiza, D., Brandt, A. R., Jackson, R. B., Hamburg, S. P., 2016. Aerial surveys of elevated hydrocarbon emissions from oil and gas production sites. Environmental Science & Technology 50 (9), 4877–4886, pMID: 27045743.
URL https://doi.org/10.1021/acs.est.6b00705

Molod, A., Takacs, L., Suarez, M., Bacmeister, J., Song, I.-S., Eichmann, A., 2012. he GEOS-5 Atmospheric General Circulation Model: Mean Climate and Development from MERRA to Fortuna. https://portal.nccs.nasa.gov/datashare/gmao/geos-fp/das/, nASA TM-2012-104606, 2012.

Pandey, S., Gautam, R., Houweling, S., van der Gon, H. D., Sadavarte, P., Borsdorff, T., Hasekamp, O., Landgraf, J., Tol, P., van Kempen, T., Hoogeveen, R., van Hees, R., Hamburg, S. P., Maasakkers, J. D., Aben, I., 2019. Satellite observations reveal extreme methane leakage from a natural gas well blowout. Proceedings of the National Academy of Sciences 116 (52), 26376–26381.
URL https://www.pnas.org/content/116/52/26376

Roberts, D. A., Bradley, E. S., Cheung, R., Leifer, I., Dennison, P. E., Margolis, J. S., 2010. Mapping methane emissions from a marine geological seep source using imaging spectrometry. Remote Sensing of Environment 114 (3), 592–606.
URL https://www.sciencedirect.com/science/article/pii/S0034425709003241

Saunois, M., Stavert, A. R., Poulter, B., Bousquet, P., Canadell, J. G., Jackson, R. B., Raymond, P. A., Dlugokencky, E. J., Houweling, S., Patra, P. K., Ciais, P., Arora, V. K., Bastviken, D., Bergamaschi, P., Blake, D. R., Brailsford, G., Bruhwiler, L., Carlson, K. M., Carrol, M., Castaldi, S., Chandra, N., Crevoisier, C., Crill, P. M., Covey, K., Curry, C. L., Etiope, G., Frankenberg, C., Gedney, N., Hegglin, M. I., Höglund-Isaksson, L., Hugelius, G., Ishizawa, M., Ito, A., Janssens-Maenhout, G., Jensen, K. M., Joos, F., Kleinen, T., Krummel, P. B., Langenfelds, R. L., Laruelle, G. G., Liu, L., Machida, T., Maksyutov, S., McDonald, K. C., McNorton, J., Miller, P. A., Melton, J. R., Morino, I., Müller, J., Murguia-Flores, F., Naik, V., Niwa, Y., Noce, S., O'Doherty, S., Parker, R. J., Peng, C., Peng, S., Peters, G. P., Prigent, C., Prinn, R., Ramonet, M., Regnier, P., Riley, W. J., Rosentreter, J. A., Segers, A., Simpson, I. J., Shi, H., Smith, S. J., Steele, L. P., Thornton, B. F., Tian, H., Tohjima, Y., Tubiello, F. N., Tsuruta, A., Viovy, N., Voulgarakis, A., Weber, T. S., van Weele, M., van der Werf, G. R., Weiss, R. F., Worthy, D., Wunch, D., Yin, Y., Yoshida, Y., Zhang, W., Zhang, Z., Zhao, Y., Zheng, B., Zhu, Q., Zhu, Q., Zhuang, Q., 2020. The global methane budget 2000–2017. Earth System Science Data 12 (3), 1561–1623.
URL https://essd.copernicus.org/articles/12/1561/2020/

Schneising, O., Buchwitz, M., Reuter, M., Vanselow, S., Bovensmann, H., Burrows, J. P., 2020. Remote sensing of methane leakage from natural gas and petroleum systems revisited. Atmospheric Chemistry and Physics 20 (15), 9169–9182.
URL https://acp.copernicus.org/articles/20/9169/2020/

Thompson, D. R., Leifer, I., Bovensmann, H., Eastwood, M., Fladeland, M., Frankenberg, C., Gerilowski, K., Green, R. O., Kratwurst, S., Krings, T., Luna, B., Thorpe, A. K., 2015. Real-time remote detection and measurement for airborne imaging spectroscopy: a case study with methane. Atmospheric Measurement Techniques 8 (10), 4383–4397.
URL https://amt.copernicus.org/articles/8/4383/2015/

Thompson, D. R., Thorpe, A. K., Frankenberg, C., Green, R. O., Duren, R., Guanter, L., Hollstein, A., Middleton, E., Ong, L., Ungar, S., 2016. Space-based remote imaging spectroscopy of the aliso canyon ch4 superemitter. Geophysical Research Letters 43 (12), 6571–6578.
URL https://agupubs.onlinelibrary.wiley.com/doi/abs/10.1002/2016GL069079

Thorpe, A. K., Frankenberg, C., Roberts, D. A., 2014. Retrieval techniques for airborne imaging of methane concentrations using high spatial and moderate spectral resolution: application to aviris. Atmospheric Measurement Techniques 7 (2), 491–506.
URL https://amt.copernicus.org/articles/7/

491/2014/

Thorpe, A. K., Frankenberg, C., Thompson, D. R., Duren, R. M., Aubrey, A. D., Bue, B. D., Green, R. O., Gerilowski, K., Krings, T., Borchardt, J., Kort, E. A., Sweeney, C., Conley, S., Roberts, D. A., Dennison, P. E., 2017. Airborne doas retrievals of methane, carbon dioxide, and water vapor concentrations at high spatial resolution: application to aviris-ng. Atmospheric Measurement Techniques 10 (10), 3833–3850.
URL https://amt.copernicus.org/articles/10/3833/2017/

United Nations Environment Programme, 2021. Global Methane Assessment: Benefits and Costs of Mitigating Methane Emissions. https://www.unep.org/resources/report/global-methane-assessment-benefits-and-costs-mitigating-methane-emissions.

Varon, D. J., Jacob, D. J., Jervis, D., McKeever, J., 2020a. Quantifying Time-Averaged Methane Emissions from Individual Coal Mine Vents with GHGSat-D Satellite Observations. Environmental Science & Technology 54 (16), 10246–10253, pMID: 32672947.
URL https://doi.org/10.1021/acs.est.0c01213

Varon, D. J., Jacob, D. J., McKeever, J., Jervis, D., Durak, B. O. A., Xia, Y., Huang, Y., 2018. Quantifying methane point sources from fine-scale satellite observations of atmospheric methane plumes. Atmospheric Measurement Techniques 11 (10), 5673–5686.
URL https://amt.copernicus.org/articles/11/5673/2018/

Varon, D. J., Jervis, D., McKeever, J., Spence, I., Gains, D., Jacob, D. J., 2020b. High-frequency monitoring of anomalous methane point sources with multispectral sentinel-2 satellite observations. Atmospheric Measurement Techniques Discussions 2020, 1–21.
URL https://amt.copernicus.org/preprints/amt-2020-477/

Varon, D. J., McKeever, J., Jervis, D., Maasakkers, J. D., Pandey, S., Houweling, S., Aben, I., Scarpelli, T., Jacob, D. J., 2019. Satellite Discovery of Anomalously Large Methane Point Sources From Oil/Gas Production. Geophysical Research Letters 46 (22), 13507–13516.
URL https://agupubs.onlinelibrary.wiley.com/doi/abs/10.1029/2019GL083798

Veefkind, J., Aben, I., McMullan, K., Förster, H., de Vries, J., Otter, G., Claas, J., Eskes, H., de Haan, J., Kleipool, Q., van Weele, M., Hasekamp, O., Hoogeveen, R., Landgraf, J., Snel, R., Tol, P., Ingmann, P., Voors, R., Kruizinga, B., Vink, R., Visser, H., Levelt, P., 2012. Tropomi on the esa sentinel-5 precursor: A gmes mission for global observations of the atmospheric composition for climate, air quality and ozone layer applications. Remote Sensing of Environment 120, 70–83, the Sentinel Missions - New Opportunities for Science.
URL https://www.sciencedirect.com/science/article/pii/S0034425712000661

Zhang, Y., Gautam, R., Pandey, S., Omara, M., Maasakkers, J. D., Sadavarte, P., Lyon, D., Nesser, H., Sulprizio, M. P., Varon, D. J., Zhang, R., Houweling, S., Zavala-Araiza, D., Alvarez, R. A., Lorente, A., Hamburg, S. P., Aben, I., Jacob, D. J., 2020. Quantifying methane emissions from the largest oil-producing basin in the united states from space. Science Advances 6 (17).
URL https://advances.sciencemag.org/content/6/17/eaaz5120